QISTA-ImageNet: A Deep Compressive Image Sensing Framework Solving ℓ_q-Norm Optimization Problem

Gang-Xuan Lin[1], Shih-Wei Hu[1], and Chun-Shien Lu[1,2][0000−0002−5900−0019]

[1] Institute of Information Science, Academia Sinica, Taiwan, ROC
[2] Research Center for Info. Technology Innovation, Academia Sinica, Taiwan, ROC
lcs@iis.sinica.edu.tw

Abstract. In this paper, we study how to reconstruct the original images from the given sensed samples/measurements by proposing a so-called deep compressive image sensing framework. This framework, dubbed QISTA-ImageNet, is built upon a deep neural network to realize our optimization algorithm QISTA (ℓ_q-ISTA) in solving image recovery problem. The unique characteristics of QISTA-ImageNet are that we (1) introduce a generalized proximal operator and present learning-based proximal gradient descent (PGD) together with an iterative algorithm in reconstructing images, (2) analyze how QISTA-ImageNet can exhibit better solutions compared to state-of-the-art methods and interpret clearly the insight of proposed method, and (3) conduct empirical comparisons with state-of-the-art methods to demonstrate that QISTA-ImageNet exhibits the best performance in terms of image reconstruction quality to solve the ℓ_q-norm optimization problem.

1 Introduction

1.1 Problem Definition and Motivation

In sparse signal recovery such as compressive sensing (CS) [8][16], we typically let $x_0 \in \mathbb{R}^n$ denote a k-sparse signal to be sensed, let $A \in \mathbb{R}^{m\times n}$ represent a sensing/sampling matrix, and let $y \in \mathbb{R}^m$ be the measurement vector defined as $y = Ax_0$, where $k < m < n$ and $\frac{m}{n}$ is the measurement rate (MR), and x_0 can be either a 1D signal or obtained from reshaping a 2D image. At the decoder, x_0 can be recovered based on its sparsity by solving the ℓ_1-norm regularization problem, which is known as "LASSO" [33][14]:

$$\text{(LASSO)} \quad \min_x \frac{1}{2}\|y - Ax\|_2^2 + \lambda \|x\|_1 , \tag{1}$$

where $\lambda > 0$ is a regularization parameter.

Nevertheless, considering that LASSO cannot recover the original sparse signal under low MRs [11], ℓ_q-norm regularization has been suggested [11][12]. The (non-convex) ℓ_q-norm regularization problem has the form

$$(\ell_q): \quad \min_x \frac{1}{2}\|y - Ax\|_2^2 + \lambda \|x\|_q^q , \tag{2}$$

where $0 < q < 1$ and $\|x\|_q = \sum_{i=1}^{n} (|x_i|^q)^{1/q}$ is the ℓ_q-quasi-norm (which is usually called ℓ_q-norm).

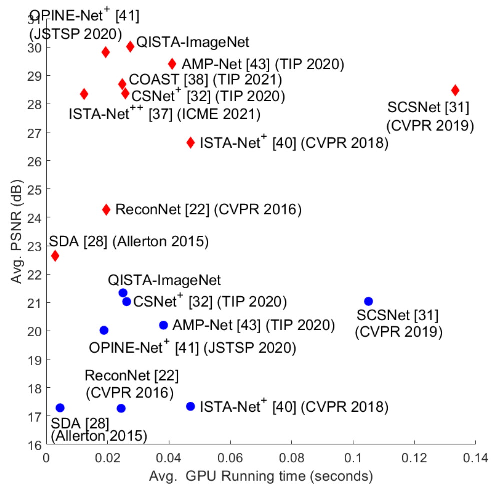

Fig. 1: Comparison of the reconstruction quality in terms of PSNR (dB) and GPU running time (in seconds) between QISTA-ImageNet and state-of-the-art methods. The average PSNR values are reconstruction results from dataset Set11 under measurement rates of 1% (in blue circle) and 10% (in red diamond), respectively. The average GPU running time is the time of reconstructing a 256×256 gray-scale image. Please note that since current learning-based CS algorithms have already achieved real-time recovery and the time actually depends on the used hardwares and programming languages, the running time results provided here were excerpted from the literautre for reference purpose only. The AMP-Net denotes the AMP-Net-9-BM version (with best results). We can see that, under the harsh environment of measurement rate 1%, QISTA-ImageNet surpass all the methods in reconstruction quality (in dB). Overall, all these methods exhibit similar tendencies under different datasets and measurement rates (see Sec. 4).

It is noted that the discussions regarding an (ℓ_q)-problem or effective algorithms for finding its optimal solution are very rare in the literature. In [23], we reformulated the non-convex ℓ_q-norm minimization problem into a 2-step problem with $q \in (0, 1)$ that is composed of one convex and one non-convex subproblems, and proposed an iterative algorithm, called QISTA (ℓ_q-ISTA), to solve 1D signal recovery from the given incomplete samples.

In this paper, we further study how to reconstruct the original images from the given sensed data (samples/measurements) by proposing a so-called deep compressive image sensing framework. Our framework is built upon and extended from QISTA that aims at 1D signal recovery [23]. Although QISTA is not designed for image recovery that is often treated as an (ℓ_1)-problem, we propose a new 2D image recovery algorithm, which is formulated as an (ℓ_q)-problem and unfolded into a new network architecture, dubbed QISTA-ImageNet, for natural image reconstruction. For image recovery from incomplete samples, Fig. 1 shows that QISTA-ImageNet, compared with the state-of-the-art methods, achieves the relatively better results in terms of reconstruction quality.

1.2 Related Works

To learn signal reconstruction, the network architecture is generated by a technique called *algorithm unfolding* [27], which unfolds specific parameters of an iterative algorithm to be learning parameters. The network architectures for 2D image reconstruction can be classified into two categories: heuristic design and algorithm unfolding. The main difference between them is that algorithm unfolding connects the network architecture with the traditional iterative algorihm, which implies the trained network is interpretable [9][17].

For the first category, Mousavi *et al.* [28] first proposed to apply a stacked denoising auto-encoder (SDA) to learn the representation and to reconstruct natural images from their CS measurements. Kulkarni *et al.* [22] further developed a CNN-based method, dubbed ReconNet, to reconstruct the natural images. Similar to [28][22], all network architectures in MS-CSNet [30], DR^2-Net [19], MSRNet [24], CSNet$^+$ [32], and SCSNet [31] are heuristic designs for solving CS. For the second category, Yang *et al.* designed a network architecture called ADMM-Net [36], where the structure of each layer is obtained by unfolding the specific parameters in the traditional iterative algorithm, ADMM [35][7]. Zhang *et al.* designed ISTA-Net and ISTA-Net$^+$ [40] by unfolding the traditional iterative algorithm ISTA [14][4]. The authors further proposed two extensions, called COAST [38] and ISTA-Net^{++} [37]. Different from ISTA-Net$^+$, COAST further designed a controllable proximal mapping module and a plug-and-play deblocking strategy to dynamically modulate the network features and effectively eliminate the blocking artifacts, respectively. Zhang *et al.* proposed a so-called OPINE-Net [41], which adopts the framework of ISTA-Net$^+$ [40] with an additional learning parameter in that it is a convolutional operator unfolded by the sampling matrix A. Zhang *et al.* proposed AMP-Net [43] inspired by two iterative algorithms, DIT and AMP [26], with an additional noise estimation. We also note that there is a branch of studies in (image) inverse problem that merges the iterative algorithm and DNN, which is the so-called plug-and-play (PnP) framework, including PnP-ADMM [10][29] and PnP proximal gradient method (PnP-PGM) [34]. However, the PnP framework is different from the framework of unfolding a traditional iterative algorithm in a DNN model in that the latter requires the traditional iterative algorithm to be presented explicitly, whereas the former does not seek to define an explicit regularization term because solving the proximal operator associated with the regularization term is impractical. Instead, both PnP-ADMM and PnP-PGM replace the proximal operator with a trained denoiser and iterate the algorithm (ADMM or PGM) until it converges. Table 1 shows the characteristics of state-of-the-art learning-based image recovery algorithms.

Table 1: Comparisons with state-of-the-art methods. FC and Conv. represent fully connected and convolutional oeprators, respectively.

Methods	Interpret-able	Sampling Matrix Training	Initialization	Deblocking Strategy	Regular-ization
ReconNet [22]	-	✓	FC	✓	-
DR^2-Net [19]	-	✓	Least square	-	-
CSNet$^+$ [32]	-	✓	Conv.	✓	-
SCSNet [31]	-	✓	Conv.	✓	-
AMP-Net [43]	✓	✓	FC	✓	-
ADMM-Net [36]	✓	-	follow ADMM	-	Data-driven
ISTA-Net$^+$ [40]	✓	-	Least square	-	Convex
OPINE-Net [41]	✓	✓	Conv.	-	Convex
OPINE-Net$^+$ [41]	✓	✓	Conv.	✓	Convex
COAST [38]	✓	-	naive solution	✓	Data-driven
QISTA-ImageNet	✓	✓	FC	✓	Non-convex

1.3 Contributions

The contributions in QISTA-ImageNet include:

1. Different from its 1D counterpart [23], QISTA-ImageNet is proposed to get approximated instead of exact solution (Sec. 3). This enables us to interpret clearly the insight of the proposed iterative method (Eq. (15)) in each iterative step.
2. By introducing a generalized proximal operator, the learning-based proximal gradient descent (PGD) together with an iterative algorithm in reconstructing images are proposed (Sec. 3.1 and Sec. 3.2).
3. Benefited from considering the ℓ_q-norm regularization problem in Eq. (8), we analyze how QISTA-ImageNet can exhibit better performances compared to state-of-the-art methods (Sec. 3.3).
4. In reconstructing the natural images, QISTA-ImageNet is empirically verified to be better than or comparable with state-of-the-art methods (Sec. 4).

2 Preliminary: (ℓ_q)-ISTA for 1D Sparse Signal Reconstruction

In sparse signal reconstruction, to achieve the same reconstruction performance, the requirement of the measurement rate of (ℓ_q)-based problem is lesser than that of (ℓ_1)-based problem. Unfortunately, because (ℓ_q)-based problem is non-convex, the algorithms that can achieve an acceptable solution are very rare in the literature. In [23], we proposed a new algorithm to solve the (ℓ_q)-problem (2). We first approximated the (ℓ_q)-problem into

$$\min_x F(x) = \frac{1}{2}\|y - Ax\|_2^2 + \lambda \sum_{i=1}^{n} \frac{|x_i|}{(|x_i| + \varepsilon_i)^{1-q}}, \tag{3}$$

where $\varepsilon_i > 0$ for all $i \in [1:n]$, then relaxed problem (3) (associated with the dimension of feasible domain) into

$$\min_{x,c} H(x,c) = \frac{1}{2}\|y - Ax\|_2^2 + \lambda \sum_{i=1}^{n} \frac{|x_i|}{(|c_i| + \varepsilon_i)^{1-q}}, \tag{4}$$

and reformulated problem (4) as a two-step problem:

$$\min_x \quad H(x, \bar{c}), \tag{5a}$$

$$\min_c \quad |H(\bar{x}, c) - H(\bar{x}, \bar{x}),|, \tag{5b}$$

where $\bar{x}$ and $\bar{c}$ are optimal solutions to problems (5a) and (5b), respectively. One can see that problem (4) is equivalent to problem (3) if $c = x$, and both the two problems (4) and (5) have the same optimal solution. On the one hand, since the problem (5a) is in the weighted-LASSO form (each component $|x_i|$ in the regularization term $\|x\|_1$ has weight $\frac{1}{(|c_i|+\varepsilon_i)^{1-q}}$), ISTA (iterative shrinkage-thresholding algorithm) was adopted to approach the optimal solution. On the other hand, the problem (5b) has a trivial optimal solution $c^* = \bar{x}$, even if the problem is non-convex. Thus, the (ℓ_q)-ISTA algorithm is derived by adopting one iterative step of ISTA (Eqs. (6b) and (6c)) and alternatively iterating with the optimal solution to problem (5b) (Eq. (6a)) as follows:

$$c^t = x^{t-1}, \tag{6a}$$

$$r^t = x^{t-1} + \beta A^T \left(y - Ax^{t-1}\right), \tag{6b}$$

$$x_i^t = \eta\left(r_i^t; \frac{\beta\lambda}{(|c_i^t| + \varepsilon_i)^{1-q}}\right), \ \forall i, \tag{6c}$$

where $\eta(\cdot;\cdot)$ is a component-wise soft-thresholding operator, defined as:

$$\eta(r_i; w_i) = sign(r_i) \cdot \max\{0, |r_i| - w_i\}. \tag{7}$$

In comparison with the traditional ℓ_q-norm minimization, the (ℓ_q)-ISTA algorithm is also found to be relatively stable for q's.

3 QISTA-ImageNet: Learning-Based Method for Reconstructing Natural Images

We describe a new method, QISTA-ImageNet, to reconstruct natural images. The image is, in general, a non-sparse signal in the space domain and exhibits a sparse representation in a transform domain (Fourier, STFT, wavelet, etc.). Let $x_0 \in \mathbb{R}^n$ be the vector representation of image $X_0 \in \mathbb{R}^{n_1 \times n_2}$, where $n = n_1 \cdot n_2$. Different from its 1D counterpart in problem (1), the traditional optimization method typically reconstructs the original image x_0 by solving the ℓ_1-norm regularization problem in LASSO form as: $\min_x \frac{1}{2} \|y - Ax\|_2^2 + \lambda \|\Psi x\|_1$, where $A \in \mathbb{R}^{m \times n}$ is the sensing matrix and $\Psi \in \mathbb{R}^{n \times n}$ is the dictionary that allows x_0 to be sparsely represented.

In our method, we consider the ℓ_q-norm regularization problem in the form

$$\min_x \frac{1}{2} \|y - Ax\|_2^2 + \lambda \|\Psi x\|_q^q , \tag{8}$$

where $0 < q < 1$. Similar to the process in deriving QISTA in Sec. 2, we can reformulate the problem (8) as a two-step problem:

$$\min_x \quad H(x, \bar{c}), \tag{9a}$$

$$\min_c \quad |H(\bar{x}, c) - H(\bar{x}, \Psi \bar{x})| , \tag{9b}$$

where $H(x,c) = \frac{1}{2} \|y - Ax\|_2^2 + \lambda \sum_{i=1}^n \frac{|(\Psi x)_i|}{(|c_i| + \varepsilon_i)^{1-q}}$, $\varepsilon_i > 0$ for all $i \in [1:n]$, and $\bar{x}$ and $\bar{c}$ are the optimal solutions to the x-subproblem (9a) and c-subproblem (9b), respectively. In the following, we describe how to solve these two sub-problems in (9) for natural image recovery.

To solve the optimal solution pair $(\bar{x}, \bar{c})$ to problem (9), first we can see that the optimal value of problem (9b) is obviously zero with the optimal solution $\bar{c} = \Psi \bar{x}$. Second, if $\Psi(\cdot)$ is a linear operator, then problem (9a) is convex, and the optimal solution can be approached via the PGD algorithm [3]. Unfortunately, the iterative process of PGD algorithm cannot be represented explicitly due to the composite function $|\Psi(x)|$. This implies the PGD algorithm cannot be implemented directly. Nevertheless, together with the proximal operator for composition with an affine mapping (Theorem 6.15 in [3]), we derive the explicit formula approaching the optimal solution to problem (9a) in Sec. 3.1.

3.1 Proximal Operator for Composite Function

In this subsection, we aim to design an explicit iterative process that solves problem (9a). In problem (9a), we can observe that the regularization term of the objective function is in the form of the composite function $\|\Psi(x)\|_{1,w} = \left(\|\cdot\|_{1,w} \circ \Psi\right)(x)$, where $\|x\|_{1,w} = \sum_{i=1}^n w_i |x_i|$ and $w_i = \frac{\lambda}{(|\bar{c}_i| + \varepsilon_i)^{1-q}}$. Therefore, the PGD algorithm [3] for solving problem (9a) has the form

$$r^t = x^{t-1} + \beta A^T \left(y - Ax^{t-1}\right), \tag{10a}$$

$$x^t = \text{prox}_{\|\Psi(\cdot)\|_{1,w}} \left(r^t\right). \tag{10b}$$

Remark that the proximal operator in Eq. (10b) is the soft-thresholding operator (Eq. (7)) provided the dictionary Ψ is an identity function [3][4]. However, since there is no useful calculus rule for computing the proximal operator of a composite function $\|\Psi(\cdot)\|_{1,w}$ for a general Ψ, Eq. (10b) cannot be written in an explicit function. To address this issue, we introduce the generalized proximal operator using the following theorem.

Theorem 31 *[3] Let $g : \mathbb{R}^n \to (-\infty, \infty]$ be a proper closed convex function, and let $f(x) = g(\mathcal{A}(x)+b)$, where $b \in \mathbb{R}^n$ and $\mathcal{A} : \mathbb{R}^{\hat{n}} \to \mathbb{R}^n$ is a linear transformation satisfying $\mathcal{A} \circ \mathcal{A}^T = \gamma \cdot I_n$ for some constant $\gamma > 0$. Then, for any $x \in \mathbb{R}^{\hat{n}}$,*

$$\mathrm{prox}_f(x) = x + \frac{1}{\gamma}\mathcal{A}^T \left(\mathrm{prox}_{\gamma g}(\mathcal{A}(x) + b) - (\mathcal{A}(x) + b)\right). \tag{11}$$

As described in Theorem 31, we can observe that if the dictionary Ψ is linear and satisfies a certain orthogonality condition, the solution to the proximal operator of $\|\Psi(\cdot)\|_{1,w}$ in Eq. (10b) can be found.

Hence, we propose to replace $g(x)$ and $\mathcal{A}(x)$ in Theorem 31 by $\|\cdot\|_{1,w}$ and $\Psi(x)$, respectively, to get

$$\mathrm{prox}_{\|\Psi(\cdot)\|_{1,w}}\left(r^t\right) = r^t + \frac{1}{\gamma_{\bar{c}}}\Psi^T \left(\eta\left(\Psi\left(r^t\right); \gamma_{\bar{c}}\right) - \Psi(r^t)\right), \tag{12}$$

where $(\gamma_{\bar{c}})_i = \frac{\lambda}{(|\bar{c}_i|+\varepsilon_i)^{1-q}}$ for all $i \in [1 : n]$ and $\frac{1}{\gamma_{\bar{c}}}$ is the component-wise reciprocal of $\gamma_{\bar{c}}$. Thus, Eq. (10) can be written as

$$r^t = x^{t-1} + \beta A^T \left(y - Ax^{t-1}\right) \tag{13a}$$

$$x^t = r^t + \frac{1}{\gamma_{\bar{c}}}\Psi^T \left(\eta\left(\Psi\left(r^t\right); \gamma_{\bar{c}}\right) - \Psi(r^t)\right). \tag{13b}$$

3.2 The Iterative Algorithm

To derive an iterative algorithm to solve problem (9), we know that the optimal solution to problem (9b) is $\bar{c} = \Psi(\bar{x})$ and the optimal solution to problem (9a) can be approached via Eq. (13). Similar to 1D signal recovery described in Eq. (6) in Sec. 2, we can design an iterative algorithm solving 2D image recovery problem (9) by replacing Eq. (6a) and Eq. (6c) with $c^t = \Psi\left(x^{t-1}\right)$ and Eq. (13b), respectively.

Moreover, since the dictionary Ψ plays the key role of sparsely representing a natural image, together with the fact that

$$\bar{x} \approx \bar{r} \tag{14}$$

provided Ψ is a linear operator satisfying a certain orthogonality condition, the optimal solution to problem (9b) is modified as $\bar{c} \approx \Psi(\bar{r})$. Remark that the validity of Eq. (14) is further illustrated in Appendix 6.1. Finally, the iterative algorithm is designed by iterating $c^t = \Psi(r^t)$ with Eq. (13) alternatively. More specifically, the iterative process at t-th iteration has the form

$$r^t = x^{t-1} + \beta A^T \left(y - Ax^{t-1}\right), \tag{15a}$$

$$c^t = \Psi\left(r^t\right), \tag{15b}$$

$$x^t = r^t + \frac{1}{\gamma_{c^t}} \Psi^T \left(\eta\left(\Psi\left(r^t\right); \gamma_{c^t}\right) - \Psi(r^t)\right), \tag{15c}$$

which is equivalent to

$$r^t = x^{t-1} + \beta A^T \left(y - Ax^{t-1}\right), \tag{16a}$$

$$x^t = r^t + \frac{1}{\hat{\gamma}} \Psi^T \left(\eta\left(\Psi\left(r^t\right); \hat{\gamma}\right) - \Psi(r^t)\right), \tag{16b}$$

where $\hat{\gamma}_i = \frac{\lambda}{\left(\left|(\Psi(r^t))_i\right| + \varepsilon_i\right)^{1-q}}$ for all $i \in [1:n]$.

3.3 Why Our Method Can Get Better Reconstructions?

We analyze the reason why the solution obtained by the iterative process (16) is closer to the original signal than ℓ_1-based method. The algorithm (16) solving the problem (9) consists of two steps, the gradient descent step (Eq. (16a)) and the truncation (shrinkage) step (Eq. (16b)).

The gradient descent step updates the point by moving the current iterative point x^{t-1} along the direction $A^T\left(y - Ax^{t-1}\right)$, which is perpendicular to the null space $\mathcal{N}(A)$ of A, with the step size β, to the updated point r^t, as shown in Fig. 2 (Left). Indeed, Eq. (16a) can be written as

$$\Psi\left(r^t\right) = \Psi\left(x^{t-1}\right) + \beta\Psi\left(A^T\left(y - Ax^{t-1}\right)\right), \tag{17}$$

in the dictionary domain (*i.e.*,, the space $\{\Psi(x); x \in \mathbb{R}^n\}$) provided Ψ is a linear operator. That is, in the dictionary domain, the gradient descent step makes updates by moving the current iterative point $\Psi\left(x^{t-1}\right)$ along the direction $\Psi\left[A^T\left(y - Ax^{t-1}\right)\right]$, which is perpendicular to $\{\Psi(x) : x \in \mathcal{N}(A)\}$, with the step size β to the updated point $\Psi(r^t)$, as shown in Fig. 2 (Right).

In the truncation step, Eq. (16b) is indeed the proximal operator of $\|\Psi(\cdot)\|_{1,w}$ in Eq. (12) with $\bar{c} = \Psi(r^t)$. As Theorem 31 indicates, Ψ is a linear operator satisfying $\Psi \circ \Psi^T = \gamma_{\bar{c}} \cdot I_n$. Thus, Eq. (16b) can be written as

$$\Psi\left(x^t\right) = \Psi\left(r^t\right) + \frac{1}{\gamma_{\Psi(r^t)}} \Psi\left(\Psi^T\left(\eta\left(\Psi\left(r^t\right); \gamma_{\Psi(r^t)}\right) - \Psi(r^t)\right)\right) \tag{18a}$$

$$= \Psi\left(r^t\right) + \frac{\gamma_{\bar{c}}}{\gamma_{\Psi(r^t)}} \left(\eta\left(\Psi\left(r^t\right); \gamma_{\Psi(r^t)}\right) - \Psi(r^t)\right) \tag{18b}$$

$$= \Psi\left(r^t\right) + \left(\eta\left(\Psi\left(r^t\right); \gamma_{\Psi(r^t)}\right) - \Psi(r^t)\right) \tag{18c}$$

$$= \eta\left(\Psi\left(r^t\right); \gamma_{\Psi(r^t)}\right). \tag{18d}$$

Eq. (18) is indeed the component-wise soft-thresholding operator operating at the point $\Psi(r^t)$ with the shrinkage parameter $\gamma_{\Psi(r^t)}$.

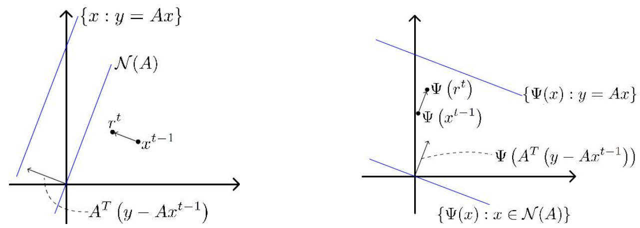

Fig. 2: Left: The gradient descent step (Eq. (16a)) in the space $\mathbb{R}^n$. Right: The gradient descent step (Eq. (17)) in the space $\{\Psi(x) : x \in \mathbb{R}^n\}$.

Moreover, in Eq. (18), the parameter $\left(\gamma_{\Psi(r^t)}\right)_i$, is determined by $|(\Psi(r^t))_i|$. We can observe that if $|(\Psi(r^t))_i|$ is non-zero or larger than the other components $\left|(\Psi(r^t))_j\right|$ (which indicates that the index i should in the support set of $\Psi(r^t)$), then $\left(\gamma_{\Psi(r^t)}\right)_i$ is relatively small and the operator $\eta\left((\Psi(r^t))_i ; \left(\gamma_{\Psi(r^t)}\right)_i\right)$ will preserve the value of $(\Psi(r^t))_i$. Conversely, if $|(\Psi(r^t))_i|$ is zero or is relatively small (which indicates that the i^{th} component of $\Psi(r^t)$ should be zero), then $\left(\gamma_{\Psi(r^t)}\right)_i$ is relatively large and the operator $\eta\left((\Psi(r^t))_i ; \left(\gamma_{\Psi(r^t)}\right)_i\right)$ will decrease the value of $|(\Psi(r^t))_i|$. As shown in Fig. 3, Eq. (18) updates the point $\Psi(r^t)$ by moving it, along the direction perpendicular to the curve $\{x : \|x\|_q = \|\Psi(r^t)\|_q\}$ (which is a contour line $\left\{x : \|x\|_q = s\right\}$ for some constant s) approximately, to approach the point $\Psi(x^t)$.

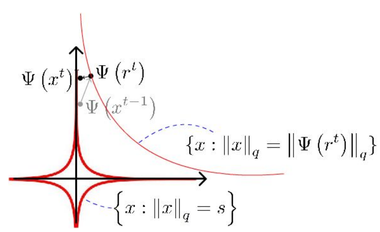

Fig. 3: The truncation step (Eq. (18)) aims at moving the point $\Psi(r^t)$ along the direction perpendicular to the curve $\left\{x : \|x\|_q = \|\Psi(r^t)\|_q\right\}$ approximately to approach the point $\Psi(x^t)$.

The above exploration reveals the insight into the iterative process (16) that gradually approaches the optimal solution to problem (8), as shown in Fig. 4. It should be noted that the parameter $\gamma_{\Psi(r^t)}$ adapts to the value of $\Psi(r^t)$ in a component-wise manner, instead of applying the same threshold to every component, as in ℓ_1-based methods such as ISTA [3][4], ISTA-Net [40], and

OPINE-Net [41]. This may explain why the solution obtained by the iterative process (16) is closer to the original signal than ℓ_1-based methods.

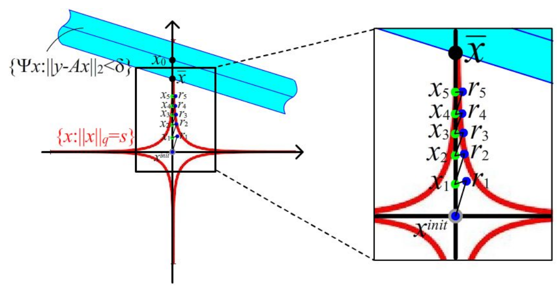

Fig. 4: The iterative process (16). The water-colored region is the set $\{\Psi(x) : \|y - Ax\|_2 < \delta\}$, where δ is a constant related to λ. The red curve is the contour line $\left\{x : \|x\|_q = s\right\}$ for a constant s. x_0 is the ground-truth and $\bar{x}$ is the optimal solution to the problem (8).

3.4 Design of Dictionary in QISTA-ImageNet Is Non-trivial

Notably, Ψ in both problem (8) and iterative algorithm (16) plays the role of a dictionary that provides an image a sparse representation. Ψ is generally treated as an over-complete dictionary (*i.e.*, $\Psi \in \mathbb{R}^{N\times n}$ with $N > n$) to achieve better representation. However, its design is not trivial, since, as $N > n$, the assumption $\Psi \circ \Psi^T = \hat{\gamma} I_N$ in Theorem 31 is not satisfied at all. Thus, it is necessary to choose a $\Psi^\dagger$ satisfying $\Psi \circ \Psi^\dagger \approx \hat{\gamma} I_N$ to replace Ψ^T. We can observe that the left-inverse of Ψ always exists, that is, $\tilde{\Psi} = \left(\Psi^T \circ \Psi\right)^{-1} \circ \Psi^T$ satisfies $\tilde{\Psi} \circ \Psi = I_n$, because $N > n$. Then, we have

$$\Psi^\dagger = I_n \circ \Psi^\dagger = \left(\tilde{\Psi} \circ \Psi\right) \circ \Psi^\dagger = \tilde{\Psi} \circ \left(\Psi \circ \Psi^\dagger\right) \approx \tilde{\Psi} \circ \hat{\gamma} I_N = \hat{\gamma}\tilde{\Psi}. \tag{19}$$

Therefore, we relax the assumption in Theorem 31 as $\frac{1}{\hat{\gamma}}\Psi^T = \bar{\gamma}\tilde{\Psi}$, where $\bar{\gamma}$ is a constant to ensure that the solution to the proximal operator in Eq. (10b) can be approximated as

$$x^t = r^t + \bar{\gamma}\tilde{\Psi}\left(\eta(\Psi(r^t); \hat{\gamma}) - \Psi(r^t)\right). \tag{20}$$

By replacing Eq. (16b) with Eq. (20), the iterative process becomes

$$r^t = x^{t-1} + \beta A^T \left(y - Ax^{t-1}\right), \tag{21a}$$

$$x^t = r^t + \bar{\gamma}\tilde{\Psi}\left(\eta\left(\Psi\left(r^t\right); \hat{\gamma}\right) - \Psi(r^t)\right). \tag{21b}$$

After imposing the above constraint of Ψ, inspired by the representation power of CNN [15] and the design of NN architecture in [40], the dictionary Ψ is adopted in the form

$$\Psi = \mathcal{C}_3 \circ \mathrm{ReLU} \circ \mathcal{C}_2 \circ \mathrm{ReLU} \circ \mathcal{C}_1 \circ \mathrm{ReLU} \circ \mathcal{C}_0 \tag{22}$$

where $\mathcal{C}_i$'s, $i = 0, 1, 2, 3$ are convolutional operators and ReLU is a rectified linear unit.

It should be noted that in order to exhibit a "left-inverse" structure of Ψ, in our design the $\tilde{\Psi}$ in Eq. (21b) is adopted in the same structure as that in Eq. (22) as

$$\tilde{\Psi} = \mathcal{C}_7 \circ \mathrm{ReLU} \circ \mathcal{C}_6 \circ \mathrm{ReLU} \circ \mathcal{C}_5 \circ \mathrm{ReLU} \circ \mathcal{C}_4 \tag{23}$$

where $\mathcal{C}_j$'s, $j = 4, 5, 6, 7$ are convolutional operators. Based on the aforementioned relaxation that $\frac{1}{\gamma_c}\Psi^T = \bar{\gamma}\tilde{\Psi}$, we will present a suitable loss function in Sec. 3.5 to ensure the left-inverse relation between Ψ and $\tilde{\Psi}$. In Appendix 6.5, we provide an ablation study on the dictionary design.

3.5 Loss Function of QISTA-ImageNet

The MSE loss

$$\mathcal{L}_{\mathrm{MSE}} = \frac{1}{n}\left\|x_0 - x^T\right\|_2^2, \tag{24}$$

where x_0 represents the ground-truth and x^T is the output of the network architecture, is typically considered in learning-based models. However, because we have relaxed $\frac{1}{\gamma_c}\Psi^T \approx \bar{\gamma}\tilde{\Psi}$, we have to impose a constraint on the left-inverse relation between Ψ and $\tilde{\Psi}$ at each layer t as

$$\mathcal{L}_{\mathrm{aux}} = \sum_{t=1}^{T}\left\|\tilde{\Psi}^t\left(\Psi^t\left(r^t\right)\right) - r^t\right\|_2^2. \tag{25}$$

Combining Eqs. (24) and (25), the loss function is designed as:

$$\mathcal{L} = \mathcal{L}_{\mathrm{MSE}} + \delta\mathcal{L}_{\mathrm{aux}}, \quad \delta > 0 \text{ is a constant.} \tag{26}$$

3.6 The Network Architecture

We construct a network architecture based on the iterative algorithm (21). Let T be the number of layers. At t^{th} layer, $t = 1, 2, \cdots, T$, with the input x^{t-1}, the output x^t is obtained by (QISTA-ImageNet):

$$r^t = x^{t-1} + \beta^t\mathcal{B}\left(y - \mathcal{A}x^{t-1}\right) \tag{27a}$$

$$x^t = r^t + \alpha^t\tilde{\Psi}^t\left(\eta(\Psi^t(r^t); \gamma^t) - \Psi^t(r^t)\right), \tag{27b}$$

where $\gamma_i^t = \frac{\lambda^t}{\left(\left|(\Psi^t(r^t))_i\right| + \varepsilon_i\right)^{1-q}}$ for all $i \in [1:n]$, and β^t, $\mathcal{B}$, $\mathcal{A}$, α^t, $\tilde{\Psi}^t$, Ψ^t and λ^t are learning parameters, which are unfolded by β, A^T, A, $\bar{\gamma}$, $\tilde{\Psi}$, Ψ, and λ, respectively. In Appendix 6.2, Fig. 5 illustrates the structure of QISTA-ImageNet.

More specifically, both $\mathcal{A}$ and $\mathcal{B}$ are fully connected operators, with the shape $m \times n$ and $n \times m$, respectively. Moreover, Ψ^t and $\tilde{\Psi}^t$ follow the structures in Eqs. (22) and (23), respectively. That is, the training parameters represented by Ψ^t and $\tilde{\Psi}^t$ are $\mathcal{C}_i^t$, $i = 0, 1, \cdots, 7$, where $\mathcal{C}_i^t$ is a convolutional operator. In summary, the learning parameters of QISTA-ImageNet are $\{\beta^t, \mathcal{B}, \mathcal{A}, \alpha^t, \lambda^t,$ and $\mathcal{C}_i^t\}_{t=1}^T$. Note that both the two learning parameters $\mathcal{A}$ and $\mathcal{B}$, which play the roles of A and A^T, respectively, in the iterative algorithm are commonly used at each layer, whereas β^t, α^t, λ^t, and C_i^t are learning parameters dependent on each layer.

Given a measurement vector y and a trained measurement matrix $\mathcal{A}$, a 2D image can be reconstructed via QISTA-ImageNet. The initial input to QISTA-ImageNet is commonly determined as

$$x^0 = \mathcal{B}y, \tag{28}$$

which plays the role of a naive initialization $A^T y$ in the iterative algorithm. In QISTA-ImageNet, instead of adopting $\mathcal{A}^T y$, the initial input is generated with the fully connected operator $\mathcal{B}$, which is independent of $\mathcal{A}$.

4 Experiments

We examine the performance of QISTA-ImageNet* in reconstructing the natural images and conduct comparison with state-of-the-art methods.

4.1 Parameters and Training Setting

The constant parameter in QISTA-ImageNet was $\varepsilon_i = 0.1$ for $i \in [1 : n]$. The training parameters of QISTA-ImageNet were initialized as $\beta^t = 0.1$, $\lambda^t = 10^{-5}$, and $\alpha^t = 1$, and $\{\mathcal{B}, \mathcal{A},$ and $\mathcal{C}_i^t, i = 0, 1, \cdots, 7\}$ were initialized using Xavier initializer [18]. All the convolutional operators $\mathcal{C}_i^t$ were set to 3×3, and the numbers of input features and output features of $\mathcal{C}_0 \sim \mathcal{C}_7$ were 32 except the numbers of input of $\mathcal{C}_0$ and output of $\mathcal{C}_7$ were set to 1. On the other hand, because $0 < q < 1$ and natural images are usually not sparse, we adopted $q = 0.5$ here Training details will be described in Appendix 6.3.

4.2 Datasets for Training and Testing

In the experiments, we follow CSNet$^+$ [32] and SCSNet [31] to use the 200 training images and 200 test images from the BSD500 database [2] as the training data. In addition, the datasets, including Set11 (11 images) [22], BSD68 (68 images) [25], Set5 (5 images) [5], Set14 (14 images) [39], and BSD100 (100 images) [25], were used for testing.

The training data were generated by cropping the gray-scale images into patches of size 64×64 with a stride of 24, and collected as a set of $91,200$

* Our code can be downloaded from https://github.com/anonymous-deep-learning/QISTA-ImageNet/

patches. Moreover, the training data were further generated by augmentation via flipping, rotation 90°, rotation 90° plus flipping, rotation 180°, rotation 180° plus flipping, rotation 270°, and rotation 270° plus flipping on each patch to yield a total of $729,600$ patches.

4.3 Performance Comparison of Natural Image Reconstruction

The experiments in this subsection were conducted on a PC with Intel Core i7-7700K CPU, a NVIDIA GeForce GTX 1080 Ti GPU, and Python with TensorFlow version 1.14.0. We compared QISTA-ImageNet with state-of-the-art learning-based methods, including SDA [28], ReconNet [22], ISTA-Net$^+$ [40], MS-CSNet [30], DR^2-Net [19], $\{0,1\}$-BCSNet [32], $\{-1,+1\}$-BCSNet [32], CSNet$^+$ [32], SCSNet [31], MSRNet [24], OPINE-Net [41], AMP-Net [43], ISTA-Net^{++} [37], COAST [38], and other methods [20][1][42]. The comparison results are shown in Table 2, Table 3, Table 4, Table 5, and Table 6, which correspond to datasets Set11, BSD68, Set5, Set14, and BSD100, respectively.

Note that the reconstruction results in Tables 2∼3 were measured in terms of PSNR, whereas the results in Tables 4∼6 of Appendix 6.4 were measured in terms of both the PSNR and SSIM [31]. This is because some prior works did not provide results for some datasets. Therefore, the "dash" mark in the tables implies that the results were not provided. In each table, the best reconstruction results are marked in bold red and the second ones are marked in bold blue. The reconstruction results in Table 2 and Table 3 indicate that QISTA-ImageNet outperforms the other methods in terms of PSNR in reconstructing Set11 and BSD68, respectively. Moreover, we can observe from Table 4, Table 5, and Table 6 that the reconstruction performance of QISTA-ImageNet in terms of PSNR outperforms the other methods in all measurement rates except for 1%. We conjecture that this is because SCSNet adopts sub-images with the size of 96×96 pixels as the input to the NN architecture, and this leads SCSNet to produce fewer blocking artifact effects. Overall, the reconstruction performance of QISTA-ImageNet in terms of SSIM is superior among all the results obtained.

In Appendix 6.4, Fig. 6, Fig. 7, and Fig. 8 show the visual comparison between the ground-truth and reconstruction results of CSNet$^+$ [32], SCSNet [31], AMP-Net-9-BM [43], OPINE-Net [41], and QISTA-ImageNet. Some methods were not selected for visual comparison as either the authors did not provide the implementation codes or [31] already offered those comparison results. As shown in Fig. 6, QISTA-ImageNet generates a relatively less blurring effect at the texture in front of the eyes of Parrot. Fig. 7 demonstrates that QISTA-ImageNet is able to reconstruct the striped texture better than other methods. Finally, Fig. 8 shows that the words "multimedia" and "presentations" are relatively recognizable in the reconstruction from QISTA-ImageNet.

5 Conclusion

We studied how to reconstruct the original images from the given sensed samples/measurements by proposing a so-called deep image sensing framework, dubbed QISTA-ImageNet. Its effectivenss has been verified through both analytic and empirical results.

Acknowledgement. This work was supported by Ministry of Science and Technology, Taiwan, ROC, under grants MOST 110-2221-E-001–020-MY2 and 109-2221-E-001–023.

Table 2: Average PSNR (dB) comparisons of different methods with various measurement rates on Set11.

Measurement rate	50%	40%	30%	25%	10%	4%	1%
SDA [28]	28.95	27.79	26.63	25.34	22.65	20.12	17.29
ReconNet [22]	31.50	30.58	28.74	25.60	24.28	20.63	17.27
[42]	36.23	34.06	31.18	30.07	24.02	17.56	7.70
LISTA-CPSS [13]	34.60	32.87	30.54	-	-	-	-
ISTA-Net$^+$ [40]	38.07	36.06	33.82	32.57	26.64	21.31	17.34
DR^2-Net [19]	-	-	-	29.06	24.71	21.29	17.80
$\{0,1\}$-BCSNet [32]	35.05	34.61	32.57	-	26.39	-	20.62
$\{-1,+1\}$-BCSNet [32]	35.57	34.94	33.42	-	28.03	-	20.93
CSNet$^+$ [32]	38.52	36.48	34.30	-	28.37	-	21.03
SCSNet [31]	39.01	36.92	34.62	-	28.48	-	**21.04**
MSRNet [24]	-	-	-	33.36	28.07	24.23	20.08
[20]	-	-	-	32.81	26.97	-	18.83
AMP-Net-9-BM [43]	**40.34**	**38.28**	**36.03**	34.63	29.40	25.26	20.20
OPINE-Net$^+$ [41]	40.19	38.11	35.96	**34.81**	**29.81**	**25.52**	20.02
ISTA-Net^{++} [37]	38.73	36.94	34.86	-	28.34	-	-
COAST [38]	38.94	37.13	35.04	-	28.69	-	-
QISTA-ImageNet	**40.87**	**38.84**	**36.64**	**35.41**	**30.01**	**26.07**	**21.34**

Table 3: Average PSNR (dB) comparisons of different methods with various measurement rates on BSD68.

Measurement rate	50%	40%	30%	25%	10%	4%	1%
SDA [28]	28.35	27.41	26.38	-	23.12	21.32	-
ReconNet [22]	29.86	29.08	27.53	-	24.15	21.66	-
ISTA-Net$^+$ [40]	34.01	32.21	30.34	-	25.33	22.17	-
CSNet [32]	34.89	32.53	31.45	-	27.10	-	22.34
SCSNet [31]	35.77	33.86	31.87	-	27.28	-	**22.37**
AMP-Net-9-BM [43]	**36.82**	**34.86**	**32.84**	**31.74**	**27.86**	**25.26**	22.28
OPINE-Net$^+$ [41]	36.32	34.33	32.46	31.50	27.81	25.16	21.88
ISTA-Net^{++} [37]	34.85	33.00	31.10	-	26.25	-	-
COAST [38]	34.74	32.93	31.06	-	26.28	-	-
QISTA-ImageNet	**37.19**	**35.15**	**33.08**	**32.03**	**28.06**	**25.43**	**22.39**

References

1. Adler, A., Boublil, D., Zibulevsky, M.: Block-based compressed sensing of images via deep learning. In Proc. Int. Workshop on Multimedia Signal Process. (MMSP) (Oct 2017) 13, 20, 21
2. Arbelaez, P., Maire, M., Fowlkes, C., Malik, J.: Contour detection and hierarchical image segmentation. IEEE Trans. Pattern Analysis and Machine Intelligence **33**(5), 898–916 (Jul 2011) 12
3. Beck, A.: First-Order Methods in Optimization. MOS-SIAM Ser. Optim. (2017) 6, 7, 9, 18
4. Beck, A., Teboulle, M.: A fast iterative shrinkage-thresholding algorithm for linear inverse problems. SIAM J. Imag. Sci. **2**(1), 183–202 (2009) 3, 6, 9, 18
5. Bevilacqua, M., Roumy, A., Guillemot, C., Alberi-Morel, M.L.: Low-complexity single-image super-resolution based on nonnegative neighbor embedding. In Proc. Brit. Mach. Vis. Conf. pp. 135–1–135–10 (2012) 12
6. Borgerding, M., Schniter, P., Rangan, S.: AMP-inspired deep networks for sparse linear inverse problems. IEEE Trans. Signal Process. **65**(16), 4293–4308 (Aug 2017) 18
7. Boyd, S., Parikh, N., Chu, E., Peleato, B., Eckstein, J.: Distributed optimization and statistical learning via the alternating direction method of multipliers. Found. Trends Mach. Learn. **3**(1), 1–122 (2011) 3
8. Candès, E.J., Romberg, J., Tao, T.: Robust uncertainty principles: exact signal reconstruction from highly incomplete frequency information. IEEE Trans. Inf. Theory **52**(2), 489–509 (2006) 1
9. Chakraborty, S., Tomsett, R., Raghavendra, R., Harborne, D., Alzantot, M., Cerutti, F., Srivastava, M., Preece, A., Julier, S., Rao, R.M., Kelley, T.D., Braines, D., Sensoy, M., Willis, C.J., Gurram, P.: Interpretability of deep learning models: A survey of results. In: IEEE SmartWorld, Ubiquitous Intell. & Comput., Adv. & Trusted Computed, Scalable Comput. & Commun., Cloud & Big Data Comput., Internet of People and Smart City Innov. (SmartWorld/SCALCOM/UIC/ATC/CBDCom/IOP/SCI). pp. 1–6 (2017) 3
10. Chan, S.H., Wang, X., Elgendy, O.A.: Plug-and-play admm for image restoration: Fixed-point convergence and applications. IEEE Trans. Comput. Imaging (Mar 2017) 3
11. Chartrand, R.: Exact reconstruction of sparse signals via nonconvex minimization. IEEE Signal Process. Lett. **14**(10), 707–710 (2007) 1
12. Chartrand, R., Yin, W.: Iteratively reweighted algorithms for compressive sensing. In Proc. Int. Conf. Acoust., Speech, Signal Process. (ICASSP) (2008) 1
13. Chen, X., Liu, J., Wang, Z., Yin, W.: Theoretical linear convergence of unfolded ISTA and its practical weights and thresholds. In Adv. Neural Inf. Process. Syst. (NeurIPS) (Dec 2018) 14
14. Daubechies, I., Defrise, M., Mol, C.D.: An iterative thresholding algorithm for linear inverse problems with a sparsity constraint. Commun. Pure Appl. Math. **57**(11), 1413–1457 (2004) 1, 3, 18
15. Dong, C., Loy, C.C., He, K., Tang, X.: Learning a deep convolutional network for image super-resolution. In Proc. Eur. Conf. Comput. Vision (ECCV) pp. 184–199 (2014) 11
16. Donoho, D.L.: Compressed sensing. IEEE Trans. Inf. Theory **52**(4), 1289–1306 (2006) 1

17. Fan, F.L., Xiong, J., Li, M., Wang, G.: On interpretability of artificial neural networks: A survey. IEEE Trans. Radiat. Plasma Med. Sci. (2021) 3
18. Glorot, X., Bengio, Y.: Understanding the difficulty of training deep feedforward neural networks. In Proc. Int. Conf. on Artif. Intell. Statist. (AISTATS) (2010) 12
19. H.Yao, Dai, F., Zhang, S., Zhang, Y., Tian, Q., Xu, C.: DR^2-Net: Deep residual reconstruction network for image compressive sensing. Neurocomputing **359**, 483–493 (Sep 2019) 3, 4, 13, 14, 20, 21
20. K., P.K.R., Chaudhury, K.N.: Learning iteration-dependent denoisers for model-consistent compressive sensing. In Proc. Int. Conf. on Image Process. (ICIP) (Sep 2019) 13, 14
21. Kingma, D.P., Ba, J.L.: Adam: A method for stochastic optimization. arXiv:1412.6980 (2014) 20
22. Kulkarni, K., Lohit, S., Turaga, P., Kerviche, R., Ashok, A.: ReconNet: Non-iterative reconstruction of images from compressively sensed measurements. In Proc. Conf. Comput. Vision Pattern Recognit. (CVPR) (Jun 2016) 3, 4, 12, 13, 14, 20, 21
23. Lin, G.X., Lu, C.S.: QISTA-Net: DNN architecture to solve ℓ_q-norm minimization problem. In Proc. Int. Workshop on Mach. Learn. Signal Process. (MLSP) (2020) 2, 4, 5
24. Liu, R., Li, S., Hou, C.: An end-to-end multi-scale residual reconstruction network for image compressive sensing. In Proc. Int. Conf. on Image Process. (ICIP) (Sep 2019) 3, 13, 14
25. Martin, D., Fowlkes, C., Tal, D., Malik, J.: A database of human segmented natural images and its application to evaluating segmentation algorithms and measuring ecological statistics. In Proc. IEEE Int. Conf. Comput. Vision (ICCV) pp. 416–423 (2001) 12
26. Metzler, C.A., Mousavi, A., Baraniuk, R.G.: Learned D-AMP: Principled neural network based compressive image recovery. In Adv. Neural Inf. Process. Syst. (NeurIPS) (Dec 2017) 3
27. Monga, V., Li, Y., Eldar, Y.C.: Algorithm unrolling: Interpretable, efficient deep learning for signal and image processing. IEEE Signal Process. Mag. **38**(2), 18–44 (Mar 2021) 3
28. Mousavi, A., Patel, A.B., Baraniuk, R.G.: A deep learning approach to structured signal recovery. In Proc. Annu. Allerton Conf. Commun., Control, and Comput. (Allerton) (Sep 2015) 3, 13, 14
29. Ryu, E., Liu, J., Wang, S., Chen, X., Wang, Z., Yin, W.: Plug-and-play methods provably converge with properly trained denoisers. In Proc. Int. Conf. Mach. Learn. (ICML) (2019) 3
30. Shi, W., Jiang, F., Liu, S., Zhao, D.: Multi-scale deep networks for image compressed sensing. In Proc. Int. Conf. on Image Process. (ICIP) (Oct 2018) 3, 13, 20, 21
31. Shi, W., Jiang, F., Liu, S., Zhao, D.: Scalable convolutional neural network for image compressed sensing. In Proc. Conf. Comput. Vision Pattern Recognit. (CVPR) (Jun 2019) 3, 4, 12, 13, 14, 19, 20, 21
32. Shi, W., Jiang, F., Liu, S., Zhao, D.: Image compressed sensing using convolutional neural network. IEEE Trans. Image Process. **29**, 375–388 (2020) 3, 4, 12, 13, 14, 19, 20, 21
33. Starck, J.L., Donoho, D.L., Candès, E.J.: Astronomical image representation by the curvelet transform. Astron. Astrophys. **398**(2), 785–800 (2003) 1
34. Sun, Y., Wohlberg, B., Kamilov, U.S.: An online plug-and-play algorithm for regularized image reconstruction. IEEE Trans. Comput. Imaging (Jan 2019) 3

35. Yang, J., Zhang, Y., Yin, W.: A fast alternating direction method for tvl1-l2 signal reconstruction from partial fourier data. IEEE J. Sel. Topics Signal Process. **4**(2), 288–297 (Apr 2010) 3
36. Yang, Y., Sun, J., Li, H., Xu, Z.: Deep admm-net for compressive sensing mri. In Adv. Neural Inf. Process. Syst. (NeurIPS) (Dec 2016) 3, 4
37. You, D., Xie, J., Zhang, J.: Ista-net^{++}: Flexible deep unfolding network for compressive sensing. In Proc. IEEE Int. Conf. Multimedia and Expo (ICME) (2021) 3, 13, 14
38. You, D., Zhang, J., Xie, J., Chen, B., Ma, S.: COAST: COntrollable Arbitrary-Sampling neTwork for compressive sensing. IEEE Trans. Image Process. **30**, 6066–6080 (2021) 3, 4, 13, 14
39. Zeyde, R., Elad, M., Protter, M.: On single image scale-up using sparse-representations. In Proc. International Conference on Curves and Surfaces pp. 711–730 (2010) 12
40. Zhang, J., Ghanem, B.: ISTA-Net: Interpretable optimization-inspired deep network for image compressive sensing. In Proc. Conf. Comput. Vision Pattern Recognit. (CVPR) (Jun 2018) 3, 4, 9, 11, 13, 14, 21
41. Zhang, J., Zhao, C., Gao, W.: Optimization-inspired compact deep compressive sensing. IEEE J. Sel. Topics Signal Process. **14**, 765–774 (May 2020) 3, 4, 10, 13, 14, 20, 21
42. Zhang, K., Zuo, W., Gu, S., Zhang, L.: Learning deep CNN denoiser prior for image restoration. In Proc. Conf. Comput. Vision Pattern Recognit. (CVPR) (Jul 2017) 13, 14
43. Zhang, Z., Liu, Y., Liu, J., Wen, F., Zhu, C.: Amp-net: Denoising-based deep unfolding for compressive image sensing. IEEE Trans. Image Process. **30**, 1487–1500 (Dec 2020) 3, 4, 13, 14, 20, 21